Meteor trail diffusion and fields: 1. Simulations

Y. S. Dimant and M. M. Oppenheim

Center for Space Physics, Boston University

Abstract. A meteoroid penetrating the Earth's atmosphere leaves behind a trail of dense plasma embedded in the lower E/upper D-region ionosphere. While radar measurements of meteor trail evolution have been collected and used to infer meteor and atmospheric properties since the 1950s, no accurate quantitative model of trail fields and diffusion exists. This paper describes finite-element simulations of trail plasma physics applicable to the majority of small meteors. Unlike earlier research, our simulations resolve both the trail and a vast current-closure area in the background ionosphere. This paper also summarizes a newly developed analytical theory of meteor electrodynamics and shows that our simulations and theory predict nearly identical fields and diffusion rates. This study should enable meteor and atmospheric researchers to more accurately interpret radar observations of specular and non-specular meteor echoes.

1. Introduction

Meteoroids have a number of important consequences for the space environment and the Earth's upper atmosphere: They damage spacecraft. They deposit material in the lower thermosphere and upper mesosphere, most notably metals and dust. They create layers of charged material which radars and ionosondes detect, modifying the plasma density and conductivity of the lower ionosphere. They leave plasma columns which can be used to monitor atmospheric conditions in the lower thermosphere and enable meteor burst communication [*Schilling*, 1993].

While large meteoroids generate spectacular optical displays, particles much smaller than a sand grain comprise the majority of all meteoroids and represent the major source of all extra-terrestrial material deposited in the Earth's atmosphere [*Bronshten*, 1983; *Ceplecha et al.*, 1998]. Such small meteoroids can rarely be observed by a naked eye or even by a sensitive optical technique, but radars can easily detect them. Such observations become possible because meteoroids frequently enter the Earth's atmosphere with a sufficient speed (11.2–72.8 km/s) [*Ceplecha et al.*, 1998] and energy to cause the formation of a dense plasma visible to radars. The front edge of this plasma can often be observed by high-power large-aperture (HPLA) radars, while smaller, lower-power radars can detect the residual trail as either specular or non-specular echoes.

Specular echoes, usually observed by small-aperture and HF-VHF radars, originate from parts of the plasma trail where the wavevector of the backscattered wave is nearly

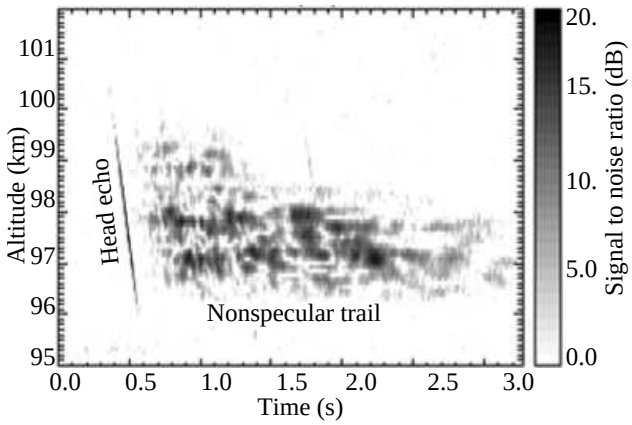

Figure 1. Non-specular radar echo (Jicamarca Radio Observatory near the magnetic equator, July 12, 2005, 3:43 AM local time).

perpendicular to the axis of a slowly diffusing, quasi-cylindrical plasma trail [*Baggaley and Webb*, 1980; *Levitskii et al.*, 1982; *Jones and Jones*, 1990; *Chilson et al.*, 1996; *Elford and Elford*, 2001; *Galligan et al.*, 2004; *Hocking*, 2004] (for review, see *Ceplecha et al.* [1998]). Non-specular meteor echoes observed by HPLA VHF or UHF radars like the one shown in Fig. 1 typically originate from trails where the radar points close to perpendicular to the geomagnetic field [*Chapin and Kudeki*, 1994; *Oppenheim et al.*, 2000; *Close et al.*, 2000; *Zhou et al.*, 2001]. Non-specular echoes appear to result from small-scale electron density irregularities caused by plasma turbulence and measured when the radar wavevector lies parallel to the irregularity wavevector but with a wavenumber twice the irregularity wavenumber, satisfying the Bragg condition [*Chapin and Kudeki*, 1994].

Modeling specular echoes requires knowledge of the spatial and temporal distribution of the plasma trail density, while modeling non-specular trails also requires knowledge of the evolution and structure of the polarization electric field which drives trail instabilities. A number of studies have looked at the evolution of dense plasma columns in collisional magnetized plasma [*Kaiser et al.*, 1969; *Pickering and Windle*, 1970]. More generally, transport phenomena in weakly ionized magnetized plasmas have been studied for many years [*Simon*, 1955a, b; *Gurevich and Tsedilina*, 1967; *Rozhanskii and Tsendin*, 1975] (for review, see *Rozhansky and Tsendin* [2001]). However, the majority of these studies were applied to moderate disturbances of a homogeneous plasma background while a meteor trail often has plasma density several orders of magnitude denser than the background plasma.

The analytical theory by *Jones* [1991] represents a significant step forward. He proposed a 2D self-similar solution (SSS) of the meteor trail evolution, starting from an initial line density. Using a combination of a Gaussian spatial distribution of the plasma density with a parabolic distribution of the electric potential, Jones developed a mathematical scheme, which describes the initial evolution and structure of the trail plasma density reasonably well. However, it improperly describes the spatial structure of the polarization electric field because the assumed plasma density structure requires that the field goes to infinity with distance from the trail axis. As we show in this paper, that theory also fails to predict significant deviations from the self-similar diffusion at a later stage of the meteor trail evolution. The reason for this is that the SSS does not account for interaction with the background ionospheric plasma (as opposed to the majority of ambipolar diffusion studies [*Gurevich and Tsedilina*, 1967; *Rozhansky and Tsendin*, 2001]).

In the earlier stage of plasma trail diffusion, the background plasma density is usually small compared to the plasma density within the trail. However, this low-density plasma plays a crucial role for carrying electric currents originating from the trail during its ambipolar diffusion. This current significantly affects the evolution and structure of the trail density in the later stage. Further, the electrodynamic interaction of the meteor trail with the background ionosphere provides a natural restriction for the polarization electric field which drives plasma instabilities. The research presented in this paper includes the interaction of the trail with the background ionosphere.

Note that in a recent theoretical paper on meteor trail diffusion, *Robson* [2001] (see also *Elford and Elford* [2001]) attempted to revise the previous theories. Robson's approach, however, has a fundamental problem. In addition to the quasineutral assumption, Robson assumed that the electron and ion fluxes along the magnetic field are equal. In the general case, the latter assumption causes the resulting electric field to have a significant non-zero curl. Estimates show, however, that the contribution of the induction electric field to the trail dynamics in the E/D regions is negligible, so that to high accuracy the electric field within and around the trail should be electrostatic, i.e., curl-free.

The earliest simulations appropriate to meteor diffusion had restricted box sizes which could not properly describe the actual ionospheric situation [*Lyatskaya and Klimov*, 1988]. In a more recent series of papers, *Oppenheim et al.* [2003a]; *Dyrud et al.* [2002]; *Oppenheim et al.* [2000]; *Dyrud et al.* [2001]; *Oppenheim et al.* [2003b]; *Dyrud et al.* [2005] have simulated the development of plasma instabilities in meteor trails when the axis of an axially-symmetric cylindrical plasma trail was perfectly aligned with the geomagnetic field or, in a two-dimensional (2D) case, making the trail a slab instead of a cylinder. This represent a severe oversimplification because most of meteor trails are oriented at a large angle with respect to the magnetic field.

In order to improve modeling of meteor trails and enhance our knowledge of plasma column diffusion and fields, we revisit this problem. As in the majority of the previous studies, we restrict ourselves to plasma columns that remain homogeneous along their length and assume constant electron and ion temperatures. Homogeneity along the trail implies that diffusion occurs only in the plane perpendicular to the trail, though electron fluxes have all three vector components. We assume that the trail axis can be directed at an arbitrary angle to the geomagnetic field and it includes the important effect of the background ionospheric plasma. Unlike previous studies, we include not only the trail, but a vast area around the trail where the currents originating in the trail close. Only such simulations can accurately describe the trail structure and accompanying electric fields. Here we include no external electric fields or strong neutral

winds which often exist in real E-region ionosphere [*Hocking*, 2004], leaving these important effects to future papers. In this paper, we present results of numerical simulations and their comparison with our analytical theory and discuss some physical implications. We present details of the analytical theory in a companion paper by *Dimant and Oppenheim* [this issue]. The combined work provides an accurate quantitative description of meteor trail evolution and the polarization electric field associated with trail ambipolar diffusion. Results of simulations and our analytical model agree remarkably well. We expect that applying our theoretical model to radar echoes from trails should help researchers obtain useful information about meteoroids and the surrounding atmosphere.

This paper is organized as follows. In Section 2, we describe the fundamental assumptions used to describe the ambipolar diffusion of meteor trails in the E-region ionosphere, introduce the concept of the residual potential, and present the governing equations for meteor fields and diffusion based on a simple two-fluid model model of a highly collisional isothermal plasma. In Section 3 we discuss results of our 2D finite-element simulations. In Section 4, we summarize the analytical results from the companion paper. In Section 5, we compare these with simulation results. In Section 6, we discuss some caveats and implications of our theory. In Section 7, we give a summary of the paper. Appendix A lists major variables used in the paper. Appendix B gives the explicit expressions for the self-similar solution, some of which we used in our simulations as the initial conditions.

2. Fundamentals of Meteor Trail Diffusion

In this section, we discuss qualitative aspects of the meteor trail diffusion and present the governing diffusion equations.

2.1. Plasma physics conditions in lower E/upper D-region ionosphere

The majority of specular and non-specular radar echoes are observed in the lower E/upper D regions at altitudes 80–120 km, where the neutral atmosphere is many orders of magnitudes denser than the ionospheric plasma. While the plasma left behind a fast meteoroid in the form of a diffusing trail can be several orders of magnitude denser than the background ionospheric plasma, it is usually much less dense than the neutral atmosphere.

All characteristic spatial scales of the diffusion state are much larger than the Debye length. The typical diffusion time scale is much longer that the electron plasma period. Due to these facts, the quasi-neutrality holds to good accuracy, $n_e \approx n_i \equiv n$, where $n_{e,i}$ are the electron and ion densities, respectively.

In the lower E/upper D region, the charged particles collide predominantly with neutral particles rather than between themselves. The following inequalities hold: $\Omega_i \ll \nu_{in}$ and $\nu_{en} \ll \Omega_e$ [*Farley*, 1985; *Dimant and Oppenheim*, 2004], where $\Omega_{e,i} = eB/m_{e,i}$ are the electron and ion gyrofrequencies; ν_{en} and ν_{in} are the electron-neutral and ion-neutral collision frequencies respectively; e is the elementary charge, $m_{e,i}$ are the electron and ion masses, respectively, and $B = |\mathbf{B}|$ where $\mathbf{B}$ is the geomagnetic flux density. The above inequalities express the fact that electrons are strongly magnetized, while ions are demagnetized due to frequent collisions with neutrals. In the equatorial region, $B \simeq 0.25 \times 10^{-4}$T, while at mid- and high latitudes $B \simeq 0.5 \times 10^{-4}$T. In the E-region ionosphere, O_2^+ and NO^+ ions dominate: $m_i \simeq 30\, m_p$, where m_p is the proton mass, so that $m_i/m_e \simeq 5.5 \times 10^4$. Throughout the upper E/lower D regions, $\nu_{en} \simeq 10\, \nu_{in}$ [*Gurevich*, 1978; *Kelley*, 1989; *Dimant and Milikh*, 2003].

2.2. Ambipolar diffusion of plasma columns

At the earliest stage of trail plasma formation, kinetic processes associated with ionization of ablated material dominate. After a short time, however, the newly formed plasma cools down, typical transport velocities become much smaller than the ion-acoustic speed, and the trail spreads over distances at least several times the characteristic mean free path [*Jones*, 1995]. This can be considered as the beginning of the diffusion stage. In this paper, we restrict our treatment to this stage.

The meteoroid velocity is usually much higher than typical diffusion velocities. This means that the trail diffusion starts roughly simultaneously over a sufficiently long distance along the trail. Considering a part of the trail which is smaller than the typical variation scale of ionospheric and neutral atmospheric parameters, we will neglect the spatial inhomogeneity and assume approximate translational symmetry along the trail axis, making all variations occur in the plane perpendicular to this axis.

We will consider the diffusion of a 2D plasma trail where the density varies with x and y and remains invariant along z (see Fig. 2). The homogeneous magnetic field $\mathbf{B}$ lies in the y, z-plane. In this geometry, the plasma density gradient, ∇n, and the electrostatic polarization electric field, $\mathbf{E} = -\nabla\Phi$, have only x and y components, while the electron drift velocity may have all three vector components.

When the trail axis lies parallel to $\mathbf{B}$, the ambipolar diffusion is axially symmetric around z and its rate roughly follows the lowest mobility [*Oppenheim et al.*, 2000]. When

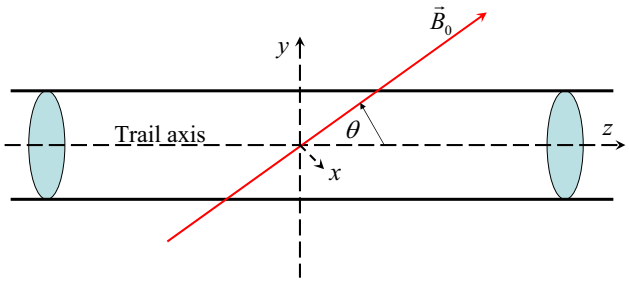

Figure 2. Geometry of the trail and magnetic field.

the trail is not aligned along $\mathbf{B}$, the ambipolar diffusion is more complicated because all components of the polarization electric field are determined by the scalar electric potential Φ. This means that the diffusion in one direction necessarily affects the diffusion in other directions. Quasineutrality requires the divergences of the electron and ion fluxes to be equal, while the fluxes themselves may differ. The combined force acting on electrons, which includes both the electric field and the pressure gradient can be represented as a gradient of a new scalar potential [*Rozhansky and Tsendin*, 2001], $-e\mathbf{E} - \nabla P_e/n = (T_e + T_i)\nabla\phi_{\rm res}$, so that

$$\phi_{\rm res} \equiv \frac{e\Phi - T_e \ln(n/n_0)}{T_e + T_i}, \tag{1}$$

where n_0 is the undisturbed ionospheric background density assumed constant and uniform. We will refer to the dimensionless quantity $\phi_{\rm res}$ as the residual potential. The concept of the residual potential is crucial for our treatment. Furthermore, the macroscopic force that drives plasma instabilities is the total force acting on electrons, which is proportional to $\nabla\phi_{\rm res}$.

2.3. Diffusion Equations

If there is no significant ionization and recombination during the diffusion stage then the plasma trail line density remains nearly constant. The diffusion stage is adequately described by fluid equations which include two inertialess momentum equations for electrons and ions, two continuity equations, and quasineutrality: $n_e \approx n_i = n$, $\nabla \cdot \mathbf{j} = 0$ [*Rozhansky and Tsendin*, 2001; *Bittencourt*, 2004], where $\mathbf{j} = en(\mathbf{V}_i - \mathbf{V}_e)$ is the current density and $\mathbf{V}_{e,i}$ are the electron and ion fluid velocities. This set of equations can be readily reduced to two coupled nonlinear partial differential equations (PDEs) for the common plasma density and the electric potential,

$$\partial_t n + \nabla \cdot \mathbf{\Gamma}_i = 0, \tag{2a}$$

$$\nabla \cdot \mathbf{\Gamma}_i - \nabla \cdot \mathbf{\Gamma}_e = 0, \tag{2b}$$

where for unmagnetized ions and strongly magnetized electrons the diffusion flux densities, $\mathbf{\Gamma}_{e,i}$, are given by

$$\mathbf{\Gamma}_i \equiv n\mathbf{V}_i = -\,n\,\frac{\nabla\left[e\Phi + T_i \ln(n/n_0)\right]}{m_i\nu_{in}}, \tag{3a}$$

$$\mathbf{\Gamma}_{e\parallel} \equiv n\mathbf{V}_{e\parallel} = n\,\frac{\nabla_\parallel\left[e\Phi - T_e \ln(n/n_0)\right]}{m_e\nu_{en}}, \tag{3b}$$

$$\mathbf{\Gamma}_{e\perp} \equiv n\mathbf{V}_{e\perp} = n\Bigg\{\frac{\nu_{en}\nabla_\perp\left[e\Phi - T_e \ln(n/n_0)\right]}{m_e\Omega_e^2} + \frac{\hat{b}\times\nabla_\perp\left[e\Phi - T_e \ln(n/n_0)\right]}{m_e\Omega_e}\Bigg\}. \tag{3c}$$

Here the subscripts $\parallel$ and $\perp$ pertain to the directions parallel and perpendicular to the magnetic field $\mathbf{B}$, respectively, and $\hat{b}$ is the unit vector in the $\mathbf{B}$ direction. The first term in the right-hand side (RHS) of Eq. (3c) describes the electron Pedersen flux, while the second term describes the electron Hall flux. Here we assume the isothermal approximation which is justified by frequent collisions with the huge thermal reservoir of neutral atmosphere (in a more general adiabatic process, we would have additional factors $\gamma_{e,i}$ in front of $T_{e.i}\ln(n/n_0)$.).

Passing from Φ to the residual potential, Eq. (1), we rewrite Eqs. (2) in the x, y coordinates as

$$\partial_t n - D\left[\nabla^2 n + \nabla\cdot(n\nabla\phi_{\rm res})\right] = 0, \tag{4a}$$

$$(1+\psi)\partial_x\left(n\partial_x\phi_{\rm res}\right) + (1+Q)\partial_y\left(n\partial_y\phi_{\rm res}\right) + \nabla^2 n + \mu\left(\partial_x\phi_{\rm res}\,\partial_y n - \partial_x n\,\partial_y\phi_{\rm res}\right) = 0, \tag{4b}$$

where we introduced the ambipolar diffusion coefficient for $m_i\nu_{in} \gg m_e\nu_{en}$ [*Bittencourt*, 2004],

$$D \equiv \frac{T_e + T_i}{m_i\nu_{in}} = \frac{(T_e + T_i)\,\Theta_0}{eB\sqrt{\psi}}, \tag{5}$$

and dimensionless parameters

$$\psi \equiv \frac{g_{e\perp}^{\rm Ped}}{g_i} = \frac{\nu_{en}\nu_{in}}{\Omega_e\Omega_i} \tag{6}$$

$$Q \equiv \psi\cos^2\theta + \frac{\sin^2\theta}{\Theta_0^2}, \tag{7}$$

$$\mu \equiv \frac{\nu_{in}\cos\theta}{\Omega_i} = \frac{\sqrt{\psi}}{\Theta_0}\cos\theta, \tag{8}$$

$$\Theta_0 \equiv \left(\frac{g_i}{g_{e\parallel}}\right)^{1/2} = \left(\frac{m_e\nu_{en}}{m_i\nu_{in}}\right)^{1/2}. \tag{9}$$

The parameter Θ_0 represents a small critical angle (in radians) which remains nearly constant throughout the upper D/lower E-region ionosphere, $\Theta_0 \simeq 1.35\times10^{-2}$ (in degrees, $\Theta_0 \simeq 0.8°$), while the parameter ψ [*Farley*, 1985] exponentially decreases as altitude increases with the e-folding

length-scale $\sim$ (2.5–3) km, see Fig. 2 in *Dimant and Oppenheim* [2004]. In our simulations, we normalized plasma to the undisturbed background density $n_0 = 1$, $n/n_0 \to n$.

3. Simulations of Trail Diffusion and Fields

In this section, we discuss general results of our numerical solution of Eq. (4) using a finite-element PDE solver FlexPDE [*FlexPDE*, 2006]. The challenge of these simulations is to simultaneously resolve both the relatively small scale of the trail density variations and the large scale of the residual potential variations parallel to the magnetic field (along y). This requires the box size along x to be at least several times the effective trail size in that direction, σ_x, while the box size along y should be at least several times the product $\Theta_0^{-1}\sigma_y$, more than two orders of magnitude larger than the box size along x. FlexPDE uses an adaptive finite element mesh to solve this highly inhomogeneous problems. In regions with rapidly changing field or density gradients it uses a high density mesh while it maintains a coarse mesh in regions with modest or uniform gradients.

In order to evaluate the effects of boundary condition on the solution, we varied the simulation box size. We also varied boundary conditions, setting either the density disturbances, $\Delta n(t) \equiv n(t) - 1$, and $\phi_{\rm res}$, or the corresponding flux densities, Eq. (3), to zero on the boundaries. These tests demonstrated that, for sufficiently large box sizes, the solution in the inner region remained essentially unaffected by the choice of boundary conditions.

In our simulations, we solved Eq. (4) with $m_i/m_e = 5.5 \times 10^5$ and $\nu_{en}/\nu_{in} = 10$. As the initial condition at time $t = t_0$, we chose a narrow and dense column of plasma, described by the self-similar solution (SSS), see Appendix B. We used normalized units where the diffusion coefficient $D = 1$ and the initial time $t_0 = 1$, so that the initial spatial distribution of the total plasma density was given by Eq. (B1) with $C = \Delta n(t_0) \equiv \Delta n_0$. For $\sin^2\theta \gg \nu_{en}/\Omega_e$, the characteristic sizes of the initial Gaussian density distribution of the trail, see Eqs. (B5) and (B7), in the x and y directions are given by $\sigma_{x0} = (2Dt_0/A_{xx})^{1/2} \approx [2\psi/(\sin^2\theta + \psi)]^{1/2}$ and $\sigma_{y0} = (2Dt_0/A_{yy})^{1/2} \approx \sqrt{2}$. They are nearly equal for $\psi \gg 1$ (lower altitudes), but differ significantly for $\psi \ll 1$ (higher altitudes). To check the effect of the initial conditions, we tried different initial Gaussian density distributions corresponding to the same trail line density. We have found that, after the time needed for the trail to diffuse over a distance several times the original size of the trail, the solution becomes virtually the same.

Equation (4b) involves no time derivatives, so that formally $\phi_{\rm res}$ needs no initial condition. However, the FlexPDE application requires setting initial conditions for all vari-

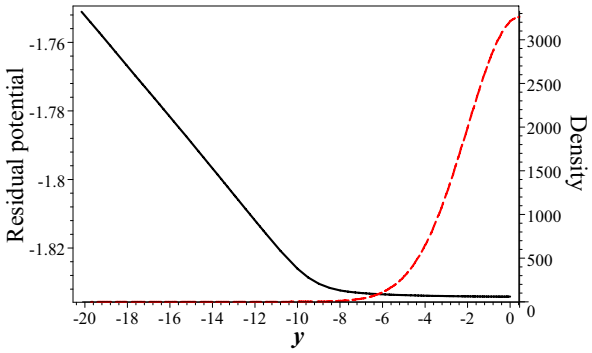

Figure 5. Typical variation parallel to the magnetic field (along y) at $x = 0$ of residual potential (solid curve, left scale) and trail density (dashed curve, right scale) [for $\psi = 0.2$, $\Delta n_0 = 10^4$, $t = 3$]. In the near-trail region, the density has exponentially strong variation along y, while the residual potential varies only within several percent of its maximum absolute value. At some point beyond the trail (here about $y = -10$), the potential acquires a noticeable y-derivative (electric field parallel to the magnetic field $\mathbf{B}$). This derivative is always much less than the typical x-derivative (electric field perpendicular to $\mathbf{B}$).

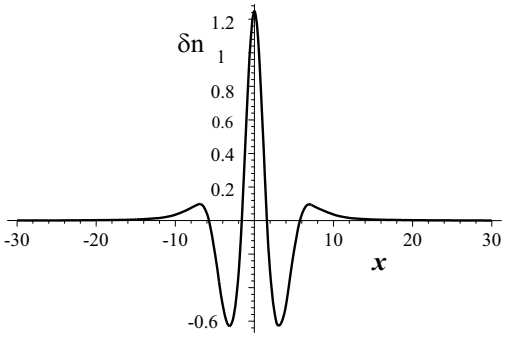

Figure 6. Disturbances of background density beyond the trail perpendicular to the magnetic field (along x) [for $\psi = 0.2$, $\Delta n_0 = 10^4$, $t = 3.5$ at the coordinate $|y| = 20$ located well beyond the trail].

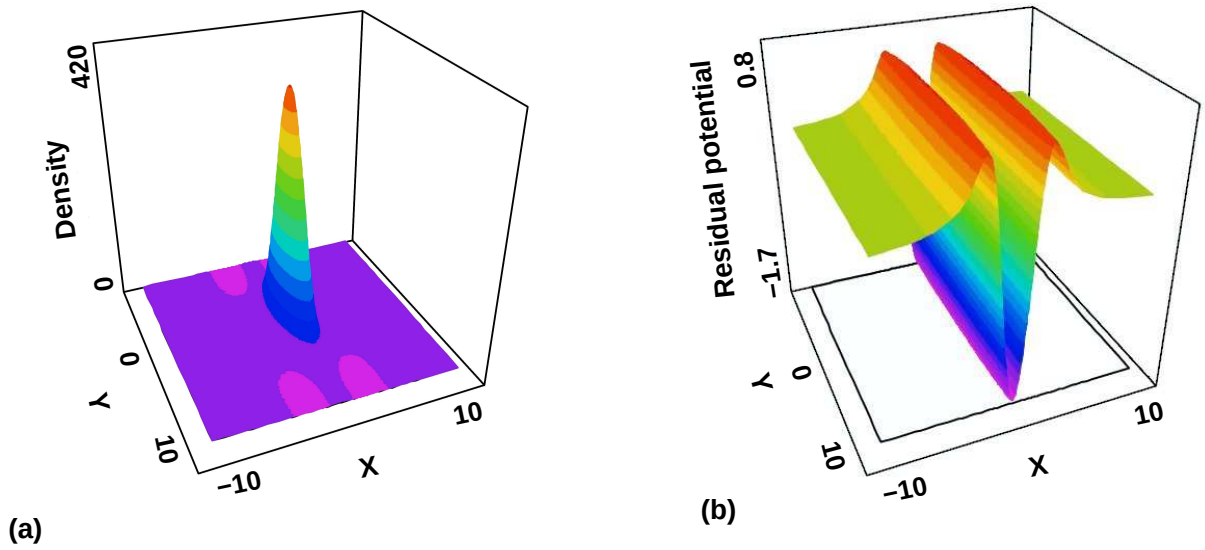

Figure 3. Typical structure of plasma density (a) and residual potential (b). Here $\psi = 0.05$, $\theta = 45°$, $\Delta n_0 = 1000$, and $t = 2.3$ (the background density corresponds to $n = 1$ and the initial time for the self-similar solution $t_0 = 1$).

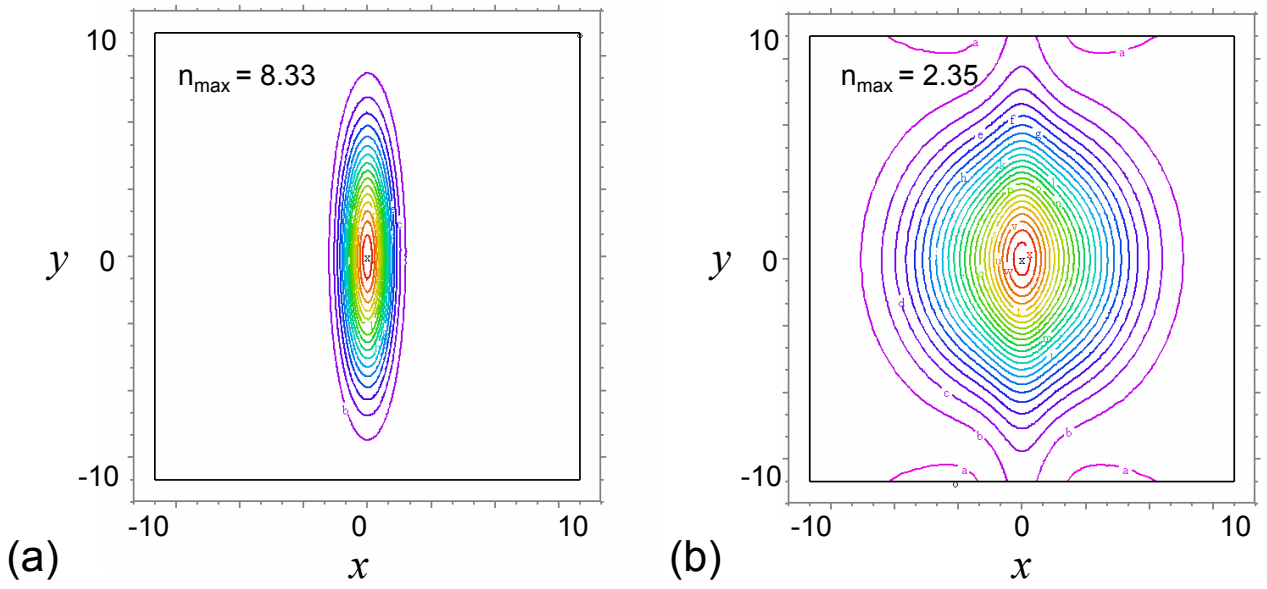

Figure 4. Contours of trail density in the x, y-plane for $\psi = 0.05$, $\Delta n_0 = 50$, $t = 6$: (a): self-similar solution, (b): simulation. Maximum densities in the trail center, $n_{\max}$, are shown.

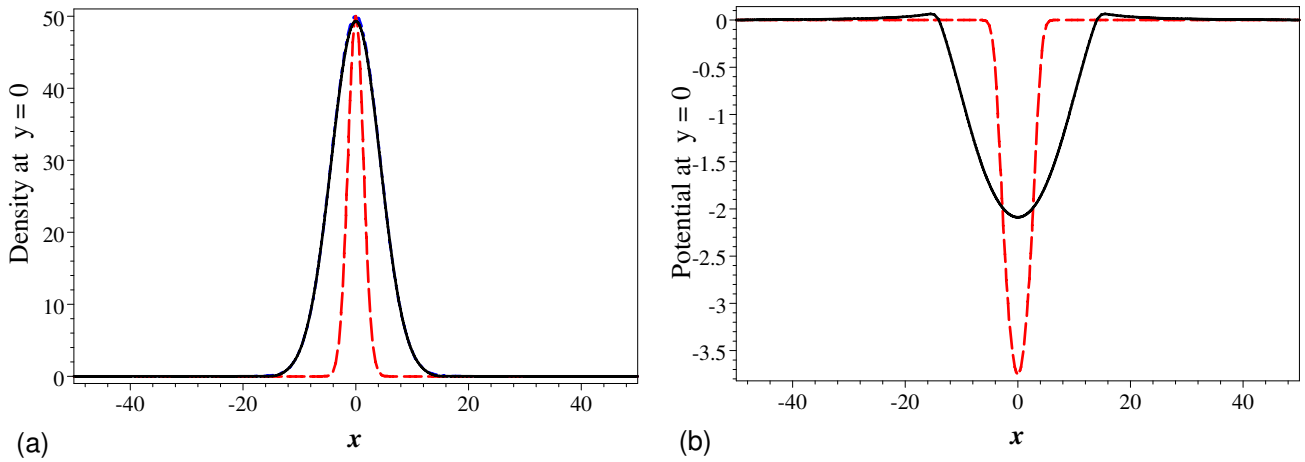

Figure 8. Plasma density (a) and residual potential (b) at $y = 0$ for $\psi = 0.05$, $\theta = 1°$, $\Delta n_0 = 1000$, and $t = 20$ (b). The solid curves show simulation results, while dashed curves show the exact solutions for the field-aligned case, $\theta = 0°$, given by Eq. (10) for the same Δn_0. The SSS for the density distribution given by Eq. (B1) is also shown in (a) by a dot-dashed curve, but is undistinguishable from simulations.

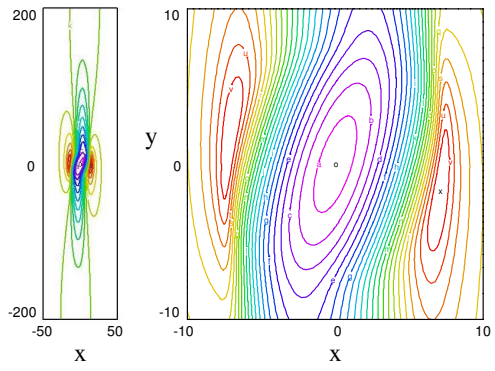

Figure 7. Contours of residual potential for a small but finite angle between the trail axis and magnetic field: $\theta = 5°$ ($\psi = 0.05$, $\Delta n_0 = 1000$). Left panel: $t = 14.5$, full box. Right panel: $t = 2.5$, only central region shown.

ables. In our simulations, we usually set up $\phi_{\rm res}(t_0) = 0$. We tested that after a rather short time, the solver automatically sets up a time-dependent spatial distribution of $\phi_{\rm res}$ which proves to be independent of the initial condition for $\phi_{\rm res}$.

While we have simulated trail evolution for different angles θ between $0°$ and $90°$, we have focused on the strictly perpendicular case, $\theta = 90°$, $\mu = 0$, because our analytical theory applies best to this case. For $\theta = 90°$, there is a mirror symmetry along both the x and y axis allowing us to only simulate a half-box along $\mathbf{B}$ ($y \leq 0$) with boundary conditions at $y = 0$ given by zero derivatives of both n and $\phi_{\rm res}$.

In order to model different stages of trail diffusion, for each set of parameters θ and ψ, we performed overlapping runs by varying the initial peak densities from $\Delta n_0 = 10^4$ to $\Delta n_0 = 10$. We finished each run at $t = 40 - 500$, so that the box size along x ($|x_{\rm max}| = 30$–60) remained at least several times $\sigma_x(t)$ and the half-box size along y, $|y_{\rm max}| = 1000$–3000, was always at least two orders of magnitude larger than $\sigma_y(t)$. This is necessary because electric fields propagate enormous distances along $\mathbf{B}$. The small ψ cases required much more time and resources than those of $\psi \gtrsim 1$ because higher anisotropies and stronger gradients develop. On a 3GHz Pentium 4 Windows-based PC, our runs lasted from several hours (for $\theta = 90°$, $\psi = 10$, $\Delta n_0 = 10$) to more than two weeks (for $\theta = 45°$, $\psi = 0.05$, $\Delta n_0 = 10^4$,

full box). FlexPDE intrinsic restrictions have not allowed us to simulate $\psi < 0.05$.

Our simulations with different angles have shown that for sufficiently large angles, $\theta \gtrsim 15^\circ$, the simulated density and residual potential look very similarly to the case of $\theta = 90^\circ$. Figure 3 shows typical plasma density and residual potential plotted over the small fraction of the simulation box nearest the trail a short time after the simulation begins. Figure 4 compares an example of the trail density contours in the x, y-plane corresponding to the SSS (a) and to the full simulation (b) after the trail has diffused to several times its initial radius. Our simulations have revealed the following major features of large-angle trail diffusion:

1 Initially, the plasma density distribution within the trail closely follows the anisotropic (for $\psi \lesssim 1$) SSS. At a later stage, the trail remains roughly Gaussian in each direction but becomes more isotropic and diffuses faster than does the SSS as shown in Fig. 4. The transition to nearly isotropic diffusion usually takes place while the peak density remains much larger than the background density.

2 The residual electric potential spreads along y well beyond the trail, see Fig. 5, with spatial gradients along y much less than those along x. Along x it has a non-monotonic symmetric structure with a deep minimum at the trail center and two symmetric maxima around it, as shown in Fig. 3(b). At the later stage, when the trail diffusion becomes nearly isotropic, the residual electric field becomes much smaller than if the density had followed the SSS.

3 Beyond the trail, where the trail density becomes much less than the background density, the residual electric field extending along $\mathbf{B}$ may substantially disturb the density as shown in Fig. 6. The field evacuates plasma from the region that maps along $\mathbf{B}$ back to the trail's potential maxima. As a result, the disturbance of background plasma evolves in antiphase to the potential distribution with a maximum at $x = 0$ and two symmetric minima roughly where the residual potential has the two maxima, as visible on the edge of Fig. 3(a). In our simulations, the maximum central density compression more than doubled the undisturbed background density, while the depletions reached about 80% of that. These strong disturbances were reached near the trail when the peak trail density was at least several orders of magnitude larger than the background density as shown in Fig. 6.

We will discuss these features in the companion paper by *Dimant and Oppenheim* [this issue], when describing our analytical theory. Here we only give brief explanations of some features.

Feature 1 In the later stage, when the peak exceeds the background density by less than a few hundred times, the gradual isotropization and acceleration of diffusion to the unmagnetized ambipolar rate result from the sharp decrease with time of the residual electric field (Feature 2). This reduction is because currents from the background plasma provide quasineutrality, instead of requiring trail electrons to follow the ions as assumed by the SSS. The resulting diffusion is mainly determined by the pressure gradient acting on the ions which are unaffected by the magnetic field.

Feature 2 The extension of the residual potential along $\mathbf{B}$, due to high parallel electron mobility, and the deep potential minimum in the trail center formed by anisotropic ambipolar trail diffusion are independent of the existence of background plasma and appear in the SSS. However, the two maxima seen in the residual potential distribution along x, see Fig. 3(b), result from particle fluxes originating in the trail and extending into the background ionosphere. The electron and ions fluxes have different and highly anisotropic patterns, though the divergences of the two fluxes remain equal. Well beyond the trail, these patterns have a quadrupole-like structures providing current closure. To drive the return currents, the background ionosphere develops potential gradients which oppose those within the trail, i.e., those responsible for the trail diffusion. This gives rise to the two symmetric potential bumps around the deep potential minimum and draws background plasma into the trail edges.

Simulations of trails with smaller angles, $\theta < 15^\circ$, shows the density closely follows the SSS for a rather long time. Within the trail area, the contours of constant density and potential are rotated in the x, y-plane due to the electron Hall drift as seen in the right panel of Fig. 7. This feature is similar to that found earlier in simulations with a small box [*Lyatskaya and Klimov*, 1988]. Beyond the trail, however, the potential is extended along y as in the large-angle case, see the left panel of Fig. 7. As θ decreases, the two-bump structure of the residual potential becomes less pronounced, although it is still visible even at $\theta = 1^\circ$ as shown in Fig. 8. As θ decreases further, $\theta \to 0$, the two-bump structure gradually disappears, and the residual potential and trail density approach the exact analytical solution for the purely field-aligned case, $\theta = 0^\circ$,

$$\phi_{\rm res} = -\frac{\ln(1+\Delta n)}{1+\psi}\,, \tag{10a}$$

$$\Delta n = \frac{N_{\rm lin}}{4\pi n_0 Dt}\,\exp\left[-\frac{(1+\psi)r^2}{4\psi Dt}\right], \tag{10b}$$

where $r^2 \equiv x^2 + y^2$. The residual potential given by Eq. (10a) has one deep minimum and no bumps, as seen in Fig. 8(b). Note that for $\psi \ll 1$ and $\theta \gtrsim 1^\circ$, the trail remains nearly isotropic but with a significantly broader spa-

tial distribution of the density and residual potential than those given by Eq. (10).

4. Summary of Analytical Results

In this section, we summarize our major analytical results from the companion paper by *Dimant and Oppenheim* [this issue]. The analytical theory has been developed for sufficiently large θ when $Q \approx \sin^2\theta/\Theta_0^2 \gg 1$, with the electron Hall term neglected. The trail density maintains an approximately anisotropic Gaussian form throughout its evolution,

$$\Delta n_{\rm Trail}(x,y,t) = \Delta n_0 \sqrt{\frac{t_0\rho(t_0)}{t\rho(t)}}\exp\left[-\frac{1}{4D}\left(\frac{\gamma x^2}{\rho(t)}+\frac{y^2}{t}\right)\right]. \tag{11}$$

To account for the time-dependant and anisotropic diffusion rates, we use a time-varying parameter $\rho(t)$ that is determined by solving

$$\gamma t = \rho + \frac{1}{1+\psi}\,\ln\left(1+\frac{1+\psi}{\psi}\,\rho\right), \tag{12}$$

or given explicitly by

$$\rho(t) = \frac{W\left(\psi e^{(1+\psi)\gamma t+\psi}\right)-\psi}{1+\psi}, \tag{13}$$

where

$$\gamma \equiv \frac{2\pi n_0(T_e+T_i)\sin\theta}{\sqrt{\psi(1+\psi)}\,N_{\rm lin}eB} \tag{14}$$

and $W(x)$ is the Lambert W-function [*Corless et al.*, 1996].

The time-dependent parameter ρ, which represents a master parameter of our analytical theory, is discussed in detail in the companion paper. Here we note that it is proportional to the square of the trail effective size in the perpendicular to $\mathbf{B}$ direction (x). It characterizes a transition from an anisotropic diffusion of the trail at early time, $\rho \ll 1$, where $\rho(t) \approx \gamma t\psi/(1+\psi)$, to a nearly isotropic diffusion at late time, $\rho(t) \gg 1$, where $\rho(t) \approx \gamma t$.

By eliminating the time dependence from Eqs. (12) and (11), one can express the peak Gaussian density, $\Delta n_{\rm Peak} \equiv \Delta n_{\rm Trail}(0,0,t)$, in terms of $\rho(t)$,

$$\Delta n_{\rm Peak} = \left\{2\Theta_0\sqrt{\rho\left[(1+\psi)\,\rho+\ln\left(1+\frac{1+\psi}{\psi}\,\rho\right)\right]}\right\}^{-1}. \tag{15}$$

The residual potential $\phi_{\rm res}(x,y,t)$ defined in Eq. (1) is also determined in terms of $\rho(t)$. In the near zone, where $|y| \ll (QDt)^{1/2}$, the potential is practically y-independent, $\phi_{\rm res}(x,y,t) \approx \phi^0_{\rm res}(x,t)$. In the earlier stage of dense-trail diffusion when $\rho(t) \approx \psi\gamma t/(1+\psi) \ll 1$, the near-zone potential can be approximated by the piece-wise function,

$$\phi^0_{\rm res}(x,t) \simeq \frac{1}{2(1+\psi)}\times\begin{cases} -\frac{\eta_0^2}{3}+\frac{\eta^2}{2} & \text{if} \quad |\eta(x,t)|<\eta_0, \\ \frac{\eta_0^4}{6\eta^2} & \text{if} \quad |\eta(x,t)|>\eta_0, \end{cases} \tag{16}$$

where $\eta(x,t) = x[\gamma/D\rho(t)]^{1/2}$ and $\eta_0 \approx 2\,[\ln(1/\rho(t))]^{1/2}$. At the later diffusion stage, $\rho(t) \gtrsim 1$, the near-zone potential is approximately given by

$$\begin{aligned}\phi^0_{\rm res}(x,t) &= \frac{1}{2(1+\psi)\rho(t)} \\ &\times \left\{S(\eta)-\frac{2\lambda(\rho)A(\rho)}{\sqrt{1+4\lambda(\rho)}}\left[\frac{4\lambda(\rho)}{1+4\lambda(\rho)}\right.\right. \\ &+ \left.\left.\left(3-2\lambda(\rho)\eta^2\right)S(\eta\sqrt{1+4\lambda(\rho)})\right]\right\},\end{aligned} \tag{17}$$

where

$$S(\eta) = -\left[\frac{i\sqrt{\pi}}{2}\,\eta e^{-\eta^2/4}\,{\rm erf}\left(\frac{i\eta}{2}\right)+1\right], \tag{18}$$

$$\lambda(\rho) = \left(\frac{\rho+c\rho^2}{40+b\rho+d\rho^2}\right)^{1/2}, \tag{19a}$$

$$A(\rho) = \left(\frac{10+N\rho}{9\rho+G\rho^2+N\rho^3}\right)^{1/2}, \tag{19b}$$

and $b \approx 122.7$, $c \approx 1.52$, $d \approx 54.74$, $N \approx 14.67$, $G \approx 29.7$. For large $\rho(t)$, in Eqs. (17) to (19) [but not in Eqs. (11) and (15)!], one should replace ρ by $\tilde\rho$ and η by $\tilde\eta(x,t) = x[\gamma/D\tilde\rho(t)]^{1/2}$, where

$$\tilde\rho = \rho\left\{\left[1+\frac{1}{(1+\psi)\rho}\ln\left(1+\frac{1+\psi}{\psi}\,\rho\right)\right]\frac{\psi}{1+\psi}\right\}^{1/2}. \tag{20}$$

For $\tilde\rho \gg 1$, the second term in the braces of Eq. (17) with $\rho,\eta \to \tilde\rho,\tilde\eta$, is small compared to $S(\tilde\eta)$ and can be neglected.

5. Comparison of Theory and Simulations

In this Section, we compare our simulations with the analytical theory summarized above. We will focus on trails at altitudes corresponding to $\psi = 0.05$–0.2 and when $\theta = 90^\circ$. In the early stage of dense-trail diffusion, $\rho \ll 1$, the analytic solution given by Eq. (11) is close to the self-similar solution (SSS) given by Eq. (B1). The density distribution from the simulations shows a nearly Gaussian peak similar to both, as seen in Fig. 9(a). However, as $\rho(t)$ increases with time and becomes of order unity, the analytic solution given by Eq. (11) starts deviating from the SSS and becomes closer to

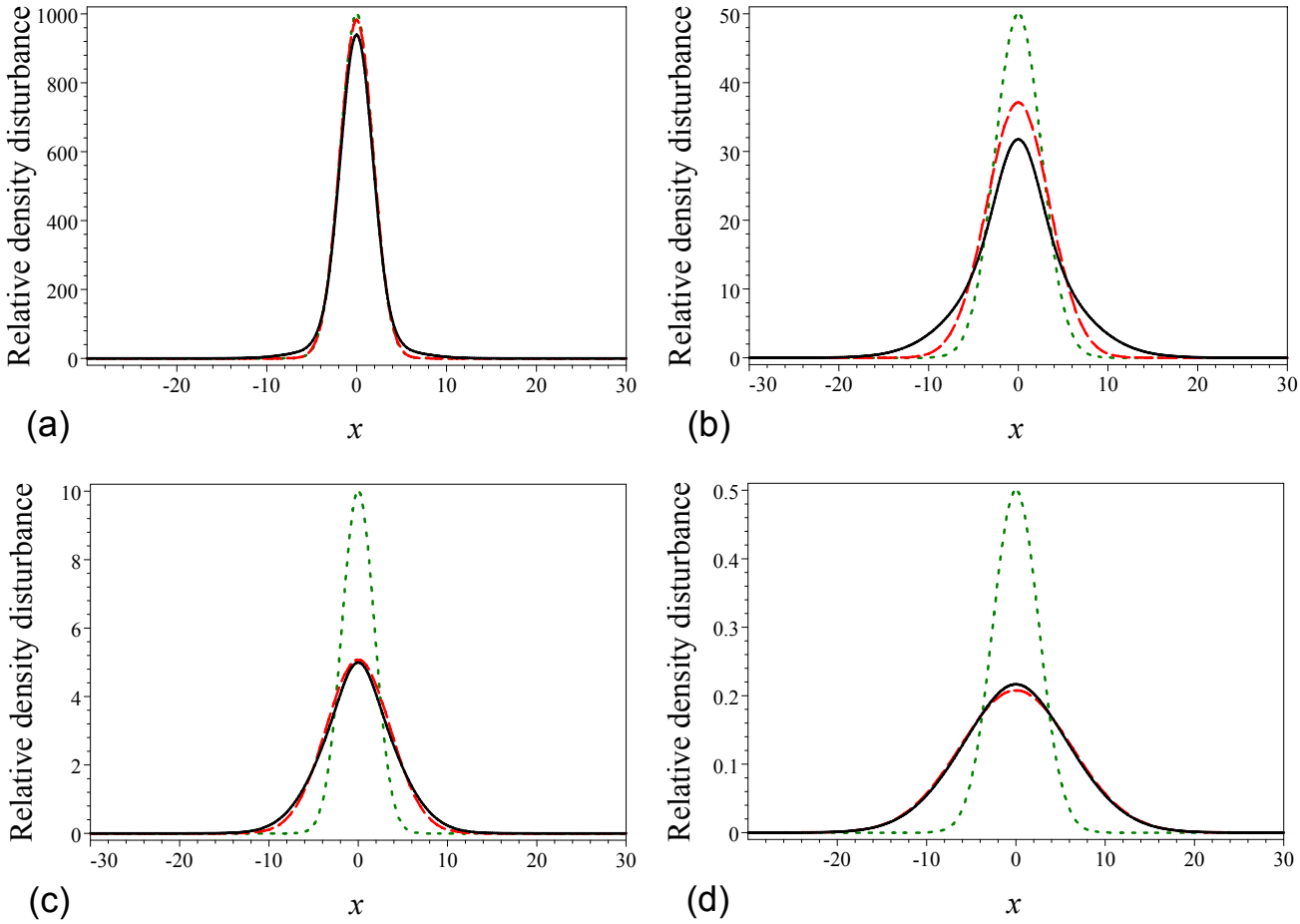

Figure 9. Trail density distribution along x for $\psi = 0.2$. (a): $\Delta n_0 = 10^4$, $t = 10$, $\rho \approx 1.4 \times 10^{-3}$. (b): $\Delta n_0 = 1000$, $t = 20$, $\rho \approx 0.5$. (c): $\Delta n_0 = 100$, $t = 10$, $\rho \approx 5.38$. (d): $\Delta n_0 = 10$, $t = 20$, $\rho \approx 160$. Solid curves: the numerical solution; dotted curves: the self-similar solution, Eq. (B1); dashed curves: the analytical solution, Eq. (11).

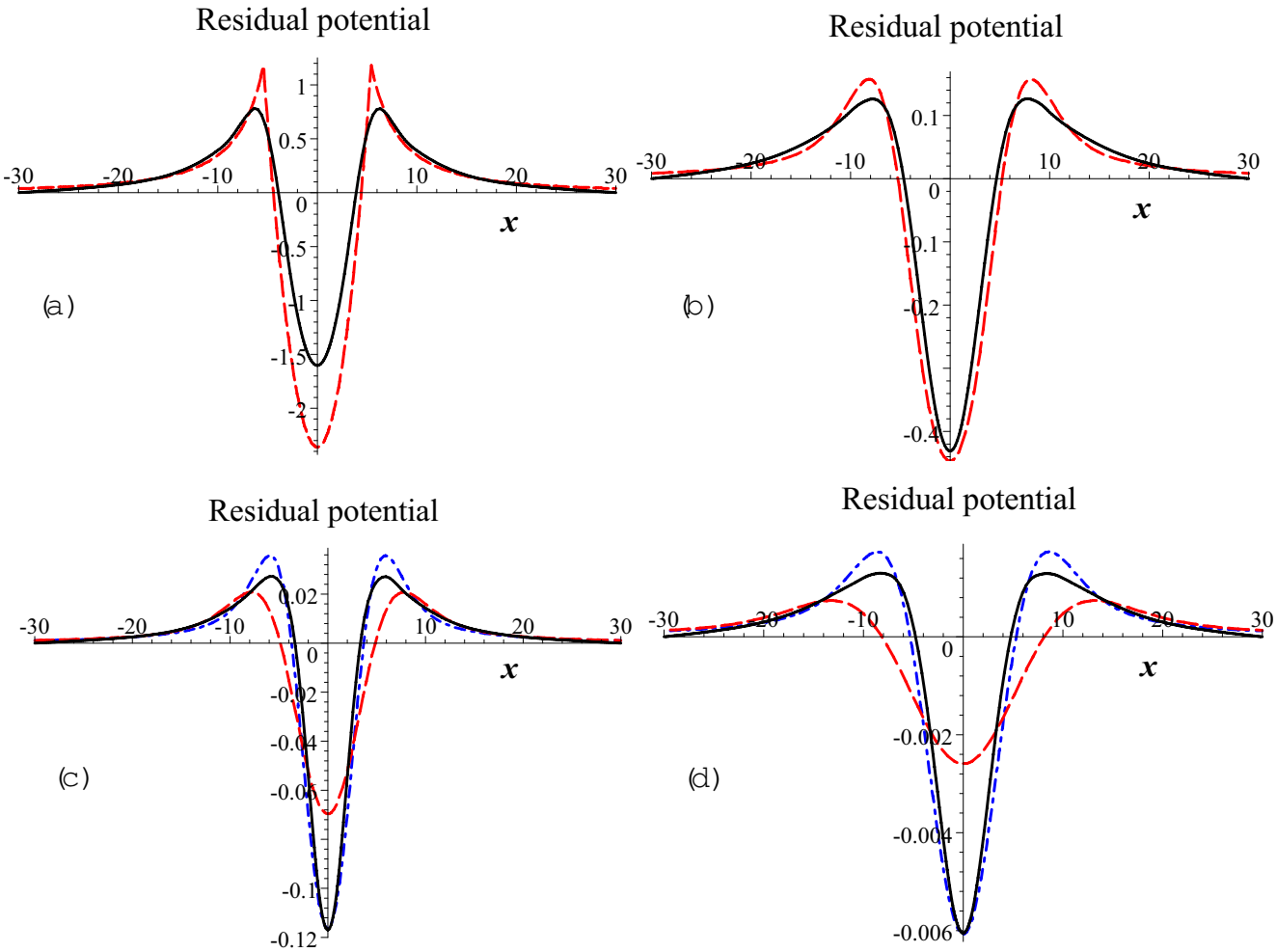

Figure 11. Residual potentials at $y = 0$, $\phi^0_{\rm res}(x,t)$, corresponding to density distributions in Fig. 9. Solid curves show the numerical solutions, while dashed and dot-dashed curves show the analytical solutions according to different equations. (a): $\Delta n_0 = 10^4$, $t = 10$, $\rho \approx 1.4 \times 10^{-3}$, dashed curve corresponds to Eq. (16). (b): $\Delta n_0 = 1000$, $t = 20$, $\rho \approx 0.5$, dashed curve corresponds to Eq. (17) with $\tilde{\rho} \to \rho$. (c): $\Delta n_0 = 100$, $t = 10$, $\rho \approx 5.38$, dashed curve corresponds to Eq. (17) with $\tilde{\rho} \to \rho$, dot-dashed curve corresponds to Eq. (17) with $\tilde{\rho} \approx 3$. (d): $\Delta n_0 = 10$, $t = 20$, $\rho \approx 160$, dashed curve corresponds to Eq. (17) with $\tilde{\rho} \to \rho$, dot-dashed curve corresponds to Eq. (17) with $\tilde{\rho} \approx 68$.

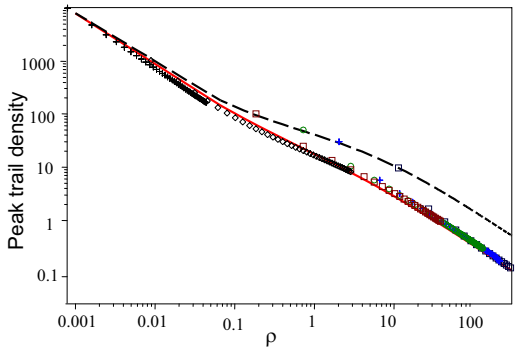

Figure 10. Peak trail density vs. parameter ρ, Eq. (13), for $\psi = 0.05$. Points shown as alternating crosses, diamonds, boxes, and circles represent the numerical solution from several runs: $\Delta n_0 = 10^4, 10^3, 100, 50, 30, 10$. For each run, the consecutive points (from left to right) correspond to $t/t_0 = 1, 2, 3 \ldots$. Solid curve shows the analytical solution given by Eq. (15). Dashed curve shows the SSS given by Eq. (B1).

the numerical solution, as illustrated in Fig. 9(b). When $\rho(t)$ becomes larger, $\rho \gg 1$, the analytical theory shows an excellent agreement with simulations, while the SSS predicts a noticeably slower diffusion, as shown in Figs. 9(c) and (d).

Figure 10 shows the peak trail densities vs. ρ taken from the simulations, analytical theory, and self-similar solution. The numerical solution is shown by separate groups of points taken from several different runs. Each run started at $t_0 = 1$ with different values of the initial peak trail density. In each group, consecutive points correspond to equidistant moments of time: $t = 1, 2, 3, \ldots$. The first point of the group always lies on the dashed curve corresponding to Eq. (B1) because the SSS was the initial condition for each run. However, starting from $t = 2$, the numerical points closely approach the theoretical curve given by Eq. (15), while the SSS solution given by Eq. (B1) remains noticeably offset. The theoretical curve overlays the numerical points for $\rho \gtrsim 1$, while for $\rho \ll 1$ it shows a slight deviation from the numerical points (see the beginning of this Section). The transition from an anisotropic diffusion to a more isotropic one occurs near the inflection point about $\rho = 1$. Notice that this takes place when the trail peak density remains well above the background plasma density, e.g., $\Delta n_{\max} \sim (\Theta_0\sqrt{\psi})^{-1} \simeq 80$ for $\psi = 0.05$.

Now we compare our simulations with the theoretical expressions for the residual potential in the near zone. Figure 11 shows the residual potential along x for the same conditions as in Fig. 9. Because the parameter ρ spans a broad range of values from small to large ones we will apply either Eq. (16) or Eq. (17). Figure 11(a) shows that for $\rho \ll 1$ the simple piece-wise approximation agrees reasonably with simulations in all areas not too close to the two positive bumps of the potential. Indeed, while there is a significant difference between the values of the potential minimum at $x = 0$, the potential derivative (the residual electric field) is the same in the inner region characterized by the parabolic dependence and occupied by the trail, see Fig. 9(a). On the other hand, a good agreement also exists well beyond the trail, where the residual potential decreases with increasing $|x|$ and the corresponding electric field changes its sign. The zero-order piece-wise approximation is rough in the transitional zone near the two potential maxima, where it has a discontinuity in the electric field. The maximum electric fields in the piece-wise formula are reached near the discontinuity points, approaching them from inside. The maximum electric fields in simulations are reached at some locations in the inner region closer to the center and hence have smaller values. Thus the simple analytical formula yields nearly correct electric fields everywhere except the transitional zones between the inner and outer regions, where it overestimates the electric field magnitude. We have attempted modeling the transitional electric field with higher-order interpolations to provide a smooth transition, but this underestimated the field. The error for the maximum electric field, however, remains within less than forty percent for all our simulations.

For $\rho \sim 1$, the theoretical expression given by Eq. (17) agrees well with simulations practically in all locations, as seen in Fig. 11(b). As ρ becomes large, Eq. (17) with unadjusted ρ shows a significant discrepancy, as seen in Fig. 11(c) and (d), while Eq. (17) with the adjusted parameter $\rho \to \tilde{\rho}$ according to Eq. (20) shows an excellent agreement. We emphasize that the adjusted parameter $\tilde{\rho}$ is only needed for the residual potential and not for the trail density.

In this section, we showed the comparison of theory and simulations mainly for small ψ. For larger values of ψ, $\psi \gtrsim 1$, simulations of trail diffusion have always shown a remarkable agreement with the analytical theory.

6. Discussion

In this section, we will briefly discuss the limitations of the theory and simulations, then we will examine the implications of our results for plasma instabilities. One limitation results from our assumption of constant electron and ion temperatures. However, the initially hot temperatures of the newly produced meteor trail plasma require time to cool. The ions cool in only a few collisions but the electrons

take much longer. This will impact the early stage diffusion. We also assumed single species plasma dominated by NO^+ and O_2^+ ions. However, meteor plasma includes multiple ion species [*Jones and Jones*, 1990; *Chilson et al.*, 1996]. Fortunately, for the singly charged ions only the mass of species is important and the mass of Si^+ is similar to NO^+ and O_2^+. Even Fe^+ is only twice as heavy, so the impact of having this range of species should be limited. We assumed homogeneity of the trail and background atmosphere along its path, allowing us to model only a 2D cross-section of the trail. This appears reasonable since trails typically extend kilometers in this direction while they are only a few 10s of meters wide in the perpendicular direction. However, the effects of trail or atmospheric density irregularities, E-region fields, or neutral winds could add inhomogeneities [*Hocking*, 2004]. Also, our analytical model approximates meteor trail diffusion where the angle between the trail and $\mathbf{B}$ is larger than a few tens of degrees, i.e., for the great majority of meteors. For smaller angles, the neglected electron Hall terms become important.

The ambipolar electric field associated with trail diffusion may drive plasma instabilities responsible for observable non-specular radar echoes. Now we estimate the driving field and instability threshold (for simplicity, for the $\theta = 90^\circ$ case). The driving field is determined by the total force acting on electrons, $\mathbf{E}_{\rm res} = -(T_e + T_i)\nabla\phi_{\rm res}$. Equations (16) to (20) give approximate analytical expressions for the residual potential. These expressions depend upon $\rho(t)$ given by Eq. (13) in terms of γ, Eq.(14), proportional to an effective trail-background interaction cross-section $\sigma_{\rm eff} \equiv N_{\rm lin}/n_0$. After a critical time, $t = t_{\rm cr}$, when $\rho(t_{\rm cr}) = 1$, the residual potential decreases drastically and the diffusion starts changing its character from the self-similar, sharply anisotropic diffusion to the nearly isotropic one. The critical time is given by

$$t_{\rm cr} = \frac{N_{\rm lin} eB\mathcal{K}(\psi)}{2\pi\,(T_e + T_i)\,n_0}\,, \tag{21}$$

where

$$\mathcal{K}(\psi) = \sqrt{\frac{\psi}{1+\psi}}\left[1 + \psi + \ln\left(\frac{1+2\psi}{\psi}\right)\right] \tag{22}$$

The critical transition time from anisotropic to isotropic diffusion is mostly relevant for high altitudes with $\psi \ll 1$, where the anisotropy of diffusion is clearly pronounced. In this case, the function $\mathcal{K}(\psi) \simeq \sqrt{\psi} \propto N_n/B$, where N_n is the neutral density. From Eq. (21) we see that $t_{\rm cr}$ is practically independent of the magnetic field, making the high- and low-latitude diffusion evolve similarly. The altitudinal dependence of $t_{\rm cr}$, however, results from it variability with N_n and the background plasma density, n_0. Nighttime E-region conditions with low n_0 for a given $N_{\rm lin}$ are equivalent to daytime conditions with a much larger n_0 requires a proportionally increased $N_{\rm lin}$ as illustrated in Fig. 12.

The strongest electric field occurs in the early diffusion stage, $\rho \ll 1$, at the edge of the nearly parabolic region of the potential, Eq. (16). According to the definition of $\phi_{\rm res}$, Eq. (1), the maximum value of the residual electric field (in real units) in this case is roughly $|E_x^{\max}| \simeq [D\gamma \ln(1/\rho)/\rho]^{1/2} m_i\nu_{in}/e(1+\psi)$, where the diffusion coefficient D is defined by Eq. (5). In the later stage of trail diffusion when $\rho \gg 1$, Eq. (17), with $\rho \to \tilde{\rho} \approx [\psi/(1+\psi)]^{1/2}\rho$ and neglected small second term in braces, gives for the maximum field $|E_x^{\max}| \simeq 0.37\,[(1+\psi)/\psi]^{3/4}\,(D\gamma/\rho)^{1/2}$ $m_i\nu_{in}/e(1+\psi)\rho$. Simple analytic interpolation between the two limits yields a formula

$$|E_x^{\max}| \simeq \frac{m_i\nu_{in}}{e(1+\psi)}\left\{\frac{D\gamma}{2\rho}\,\ln\left[1 + \frac{0.27}{\rho^2}\left(\frac{1+\psi}{\psi}\right)^{3/2}\right]\right\}^{1/2} \tag{23}$$

which is roughly valid in the entire domain of ρ.

Now we estimate the Farley-Buneman (FB) instability criterion [*Farley*, 1963; *Buneman*, 1963]. For a homogeneous plasma, the simplest FB instability criterion, obtained using the two-fluid plasma model for sufficiently long-wavelength waves, is given by $|\mathbf{V}_0| > (1+\psi)C_s$ [*Farley*, 1985], where $\mathbf{V}_0 = \mathbf{E}_{\rm res} \times \mathbf{B}/B^2$ is the $\mathbf{E}_{\rm res} \times \mathbf{B}$ drift velocity and $C_s \equiv [(T_e + T_i)/m_i]^{1/2} = (D\nu_{in})^{1/2}$ is the ion-acoustic speed. Applying this criterion to the maximum field given by Eq. (23), expressing the corresponding drift speed as $|\mathbf{V}_0| = e|E_x^{\max}|/m_i\Omega_i$, and using Eqs. (6) and (9), we write the FB instability criterion as $|E_x^{\max}| > (1+\psi)(D\nu_{in})^{1/2}(m_i\Omega_i/e)$. Expressing $E_x^{\max}$ in $N_{\rm lin}$, we reduce the FB instability criterion to

$$\frac{1}{\rho}\,\ln\left[1 + \frac{0.27}{\rho^2}\left(\frac{1+\psi}{\psi}\right)^{3/2}\right] > P, \tag{24}$$

where

$$P = \frac{\Theta_0\,(1+\psi)^{9/2}\,(eB)^2\,N_{\rm lin}}{\pi\,(T_e + T_i)\,m_i n_0}\,. \tag{25}$$

If this criterion is satisfied when the trail initially forms, then the instability starts generating plasma irregularities. If the instability persists for the sufficient time, then turbulence will develop and partially saturate through nonlinear processes. Because $\rho(t)$ monotonically increases with time then at some moment, $t = t_{\rm FB}$, the two sides of Eq. (24) become equal. At this moment, the linear growth of the FB instability starts being replaced by linear damping and irregularities will diffuse away. At $t < t_{\rm FB}$, the linear FB instability sustain plasma turbulence at a certain level, while at $t > t_{\rm FB}$

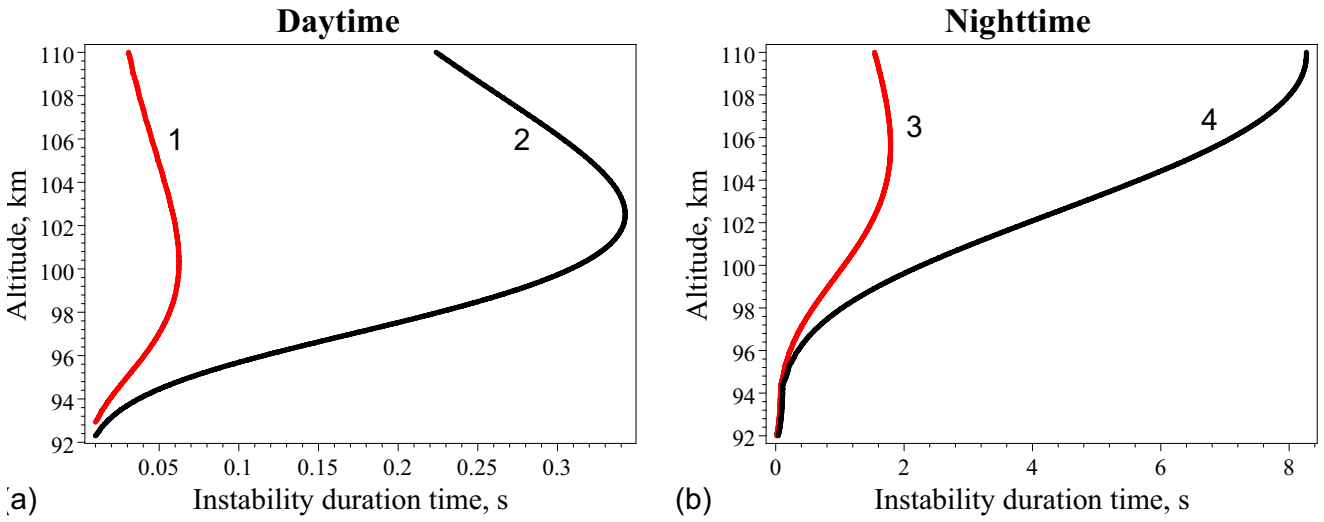

Figure 12. Altitudinal dependence of FB instability duration $t_{\rm FB}$ for the equatorial E region during (a) daytime ($n_0 = 10^{11}{\rm m}^{-3}$), where curve 1 is for $N_{\rm lin} = 10^{14}{\rm m}^{-1}$ and curve 2 is for $N_{\rm lin} = 10^{15}{\rm m}^{-1}$, and (b) nighttime ($n_0 = 10^{9}{\rm m}^{-3}$), where curve 3 is for $N_{\rm lin} = 10^{14}{\rm m}^{-1}$ and curve 4 is for $N_{\rm lin} = 10^{15}{\rm m}^{-1}$. Curves 1, 2, 3, and 4 correspond to $\sigma_{\rm eff} = 10^3,\ 10^4, 10^5$, and $10^6{\rm m}^2$, respectively.

there is no more free energy to sustain the turbulence, so that irregularities will quickly disappear.

The instability duration $t_{\rm FB}$ depends critically upon the altitudinal parameter ψ and the effective trail-background interaction cross-section $\sigma_{\rm eff} \equiv N_{\rm lin}/n_0$. Due to this, the nighttime conditions with low n_0 will produce longer lived meteor trail than will the daytime conditions. Figure 12 shows the altitude dependence of the instability duration $t_{\rm FB}$ for several constant $\sigma_{\rm eff}$ during daytime and nighttime conditions. Notice clear peaks of $t_{\rm FB}$ at some intermediate altitudes which increase with $\sigma_{\rm eff}$. The non-specular echo boundary for a given trail, like that in Fig. 1, should roughly follow the altitude dependence of $t_{\rm FB}$. However, because column plasma density varies along the meteor trail and due to other inhomogeneities, we expect more variability than this model predicts. Measurements of the evolution of the trail echoes, in combination with other observations, should enable us to retrieve useful information about meteors, ionosphere and atmosphere. Implementation of this procedure requires better models of instability generation than that used above, as well as models of ablation and ionization to give improved estimates of $N_{\rm lin}$ [*Dyrud et al.*, 2002, 2005].

7. Summary

In this paper, we have described finite-element simulations of meteor trail diffusion and fields and compared these results with an analytical theory developed in the companion paper by *Dimant and Oppenheim* [this issue]. Unlike previous models, our simulations and theory applies to trails not aligned with the geomagnetic field and includes both the trail and the background plasma in a region large enough to incorporate the current-closure area well beyond the trail. In our simulations, we have overcome the computational difficulties by employing FlexPDE, a finite-element PDE solver that uses adaptive cell structure. This has led to a better understanding of meteor diffusion which should lead to improved methods of analyzing radar data in order to remotely retrieve information about meteors and the surrounding atmosphere.

Our simulations and theory predict strong fields in the direction perpendicular to $\mathbf{B}$. These fields reverse direction just outside the trail, propagate a long distance along $\mathbf{B}$, modify diffusion rates, and can generate deep depletions in the background plasma considerable distances along $\mathbf{B}$. Comparing the simulation results with those from our analytical theory described in the companion paper demonstrate good quantitative agreement.

We also see a transition from a sharply anisotropic (for $\psi \ll 1$) diffusion to a nearly isotropic one as the effects of

currents in the background plasma become important. We predict that this transition time is proportional to the ratio of the meteor plasma density to the background density and depends on the altitude (see Eq. 21). During the day, when the background ionospheric density is high ($n_0 \sim 10^5\,\mathrm{cm}^{-3}$), this transition will occur in less than a second for most meteors, but at night ($n_0 \sim 10^3\,\mathrm{cm}^{-3}$), it can take many seconds to 10s of seconds. This is important for plasma instabilities responsible for non-specular radar echoes and for interpreting specular radar echoes as diffusion rates.

Acknowledgments. Work was supported by National Science Foundation Grants No. ATM-9986976, ATM-0332354, and ATM-0334906. Authors thank L. Dyrud and T. Lin for their help and fruitful discussions.

Appendix A: List of Major Variables

Below, in the tabular form, we list major non-standard notations used in the text and figures. If the variable definition is compact then we reproduce it in the left column. If the notation is cumbersome, we only cite in the right column the original equation for the definition. In the right column, *e*, *i*, and *n* stand for 'electron', 'ion', and 'neutral', respectively.

θ	angle between $\mathbf{B}$ and trail axis
$\Omega_{e,i} = eB/m_{e,i}$	*e* and *i* gyrofrequencies
ν_{en}, ν_{in}	*e*-*n* and *i*-*n* collision frequencies
$n = n_i \approx n_e$	quasineutral plasma density
n_0	background plasma density
$\Delta n = n/n_0 - 1$	relative density disturbance
Δn_0	initial trail density
$N_{\rm lin}$	plasma trail line density
$D = (T_e + T_i)/m_i\nu_{in}$	diffusion coefficient, Eq. (5)
$\mathbf{\Gamma}_i$, $\mathbf{\Gamma}_{e\parallel}$, $\mathbf{\Gamma}_{e\perp}$	*i* and *e* flux densities, Eq. (3)
$\phi_{\rm res}(x,y)$	residual potential, Eq. (1)
$\phi^0_{\rm res}(x)$	$\phi_{\rm res}$ in near zone, $\lvert y\rvert \ll \sqrt{QDt}$
$\psi = \nu_{en}\nu_{in}/\Omega_e\Omega_i$	altitude parameter, Eq. (6)
$Q = \psi\cos^2\theta + \frac{\sin^2\theta}{\Theta_0^2}$	*e*-mobility parameter, Eq. (7)
$\mu = \sqrt{\psi}\cos\theta/\Theta_0$	electron Hall parameter, Eq. (8)
$\Theta_0 = (m_e\nu_{en}/m_i\nu_{in})^{1/2}$	critical angle (in radians), Eq. (9)
γ	trail density parameter, Eq. (14)
$\rho(t)$	trail diffusion parameter, Eq. (13)
$\tilde\rho(t)$	adjusted $\rho(t)$, Eq. (20)
$\eta(x,t) = [\gamma/D\rho(t)]^{1/2}x$	renormalized x-coordinate
$\tilde\eta(x,t) = [\gamma/D\tilde\rho(t)]^{1/2}x$	adjusted $\eta(x,t)$
$\eta_0 \approx 2[\ln(1/\rho(t))]^{1/2}$	auxiliary parameter, Eq. (16)
$S(\eta)$, $\lambda(\rho)$, $A(\rho)$	auxiliary functions, Eq. (18).

Appendix B: Self-Similar Solution of Meteor Diffusion

In this Appendix, we obtain explicit expressions for the meteor trail diffusion in the absence of ionospheric plasma. This self-similar solution (SSS) was proposed in the general form by *Jones* [1991], but not found explicitly. We use the SSS as initial conditions for our simulations and for comparison purposes. In our notations, the SSS density and residual potential take the form

$$n^{\rm ss}(x,y,t) = \frac{C}{t}\exp\left(-\frac{A_{xx}x^2 + A_{yy}y^2 + A_{xy}xy}{4Dt}\right), \tag{B1}$$

$$\phi^{\rm ss}_{\rm res}(x,y,t) = \frac{B_{xx}x^2 + B_{yy}y^2 + B_{xy}xy}{4Dt} + \mathrm{const}, \tag{B2}$$

with positive diagonal coefficients A_{ii}, B_{ii} and

$$A_{xx}A_{yy} > \frac{A_{xy}^2}{4}, \qquad B_{xx}B_{yy} > \frac{B_{xy}^2}{4}. \tag{B3}$$

This form provides a unique and self-consistent solution to Eq. (4) in an infinite and homogeneous neutral atmosphere with no background plasma, provided the diffusion starts from an infinitely thin and dense plasma column with a given line density. The electron Hall velocities give rise to the non-diagonal coefficients, $A_{xy} = B_{xy}$. Inequalities given by Eq. (B3) mean that the contours of the constant density and the residual potential form ellipses in the xy-plane, whose major axes are rotated with respect to the x and y axes through a common angle χ determined by $\tan 2\chi = A_{xy}/(A_{xx} - A_{yy}) = B_{xy}/(B_{xx} - B_{yy})$. By assuming conserved total line density, $N_{\rm lin}$, the constant C in (B1) becomes

$$C = \frac{\left(4A_{xx}A_{yy} - A_{xy}^2\right)^{1/2}}{8\pi D}\,\frac{N_{\rm lin}}{n_0}. \tag{B4}$$

For arbitrary anisotropic particle mobilities, it is hard to obtain explicit analytical expressions for the coefficients A_{ij} and B_{ij} [*Jones*, 1991]. However, under lower E/upper D-region conditions, when electrons are strongly magnetized, while ions are unmagnetized, one can obtain such expressions. After cumbersome but straightforward algebra we obtain

$$A_{xx} = 1 + B_{xx}, \quad A_{yy} = 1 + B_{yy}, \quad A_{xy} = B_{xy}, \tag{B5}$$

$$\begin{aligned} B_{xx} &= \frac{Q\left(2+Q+\psi\right)^2 + 2\mu^2\left(Q+\psi\right)}{Q\psi\left(2+Q+\psi\right)^2 + \mu^2\left(Q+\psi\right)^2}, \\ B_{yy} &= \frac{\psi\left(2+Q+\psi\right)^2 + 2\mu^2\left(Q+\psi\right)}{Q\psi\left(2+Q+\psi\right)^2 + \mu^2\left(Q+\psi\right)^2}, \\ B_{xy} &= \frac{2\mu(2+Q+\psi)(\psi-Q)}{Q\psi(2+Q+\psi)^2 + \mu^2(Q+\psi)^2}. \end{aligned} \tag{B6}$$

The rotational angle χ is determined by $\tan 2\chi = 2\sqrt{\psi}\cos\theta/[(2+Q+\psi)\Theta_0]$. These general expressions cover all angles from $\theta = 0^\circ$ (field-aligned trail), when $Q = \psi$, $B_{xx} = B_{yy} = 1/\psi$, $B_{xy} = 0$, to $\theta = 90^\circ$ when $\mu = 0$.

Assuming $\sin^2\theta \gg \nu_{en}/\Omega_e = \Theta_0\sqrt{\psi}$, we obtain much simpler expressions for the coefficients B_{ik}:

$$B_{xx} = \frac{\sin^2\theta}{\psi},$$
$$B_{yy} = \frac{1+\cos^2\theta}{Q} = \Theta_0^2\left(\frac{1+\cos^2\theta}{\sin^2\theta}\right), \qquad \text{(B7)}$$
$$B_{xy} = -\frac{2\mu}{Q}\,\frac{\sin^2\theta}{\psi} = -\frac{2\Omega_i}{\nu_{in}}\cos\theta.$$

The non-diagonal coefficients, $A_{xy} = B_{xy}$, are small compared to A_{xx} (but not necessarily to B_{xx}!), $A_{yy} \approx 1$ and $B_{yy} \ll 1$. The rotation angle χ is small, $|\tan 2\chi| \approx 2\nu_{en}\cos\theta/(\Omega_e\sin^2\theta)$. Because $A_{xy}^2 \ll 4A_{xx}A_{yy}$ we have

$$C \approx \frac{N_{\rm lin}}{4\pi D n_0}\left(1+\frac{\sin^2\theta}{\psi}\right)^{1/2}. \qquad \text{(B8)}$$

The residual potential is stretched along the coordinate y in accord with the qualitative discussion in Sect. 2.

To the same accuracy, the particle fluxes are given by

$$\Gamma_{ex} = \Gamma_{ix} = \frac{x}{2t}\,n^{\rm ss}(x,y,t), \quad \Gamma_{ey} = \Gamma_{iy} = \frac{y}{2t}\,n^{\rm ss}(x,y,t),$$
$$\Gamma_{iz} = 0, \qquad \Gamma_{ez} = -\frac{\Omega_e}{\nu_{en}}\left(\frac{x\sin\theta}{2t}\right)n^{\rm ss}(x,y,t). \qquad \text{(B9)}$$

The flux components in both x and y directions are equal for electrons and ions. The only disparity is in the flux component along the z-axis due to electron Hall velocity. The net electric current is directed along the trail axis with the current density

$$j_z = \frac{e\Omega_e}{\nu_{en}}\left(\frac{x\sin\theta}{2t}\right)n^{\rm ss}(x,y,t). \qquad \text{(B10)}$$

This simple expression allows one to estimate the magnetic field perturbations caused by the trail and the contribution of the induction field to the electric field. For the trail peak density $n_{\max} \ll 10^{17}\,{\rm m}^{-1}$, the induction electric field will be negligible.

References

Baggaley, W. J., and T. H. Webb (1980), The geomagnetic control of the diffusion of meteoric ionozation, *Planet. Space Sci.*, *28*, 997–1001.

Bittencourt, J. A. (2004), *Fundamentals of Plasma Physics*, Springer, New York.

Bronshten, V. A. (1983), *Physics of Meteoric Phenomena*, Reidel Publishing Company, Dordrecht-Boston-Lancaster.

Buneman, O. (1963), Excitation of field aligned sound waves by electron streams, *Phys. Rev. Lett.*, *10*, 285–288.

Ceplecha, Z., J. Borovicka, W. G. Elford, D. O. Revelle, R. L. Hawkes, V. Porubcan, and M. Simek (1998), Meteor phenomena and bodies, *Space Science Reviews*, *84*, 327–471.

Chapin, E., and E. Kudeki (1994), Plasma-wave excitation on meteor trails in the equatorial electrojet, *Geophys. Res. Lett.*, *21*, 2433–2436.

Chilson, P. B., P. Czechowsky, and G. Schmidt (1996), A comparison of ambipolar diffusion coefficients in meteor trains using VHF radar and UV lidar, *Geophys. Res. Lett.*, *23*, 8937–8949.

Close, S., S. M. Hunt, M. J. Minardi, and F. M. McKeen (2000), Analysis of Perseid meteor head echo data collected using the Advanced Research Projects Agency Long-Range Tracking and Instrumentation Radar (ALTAIR), *Radio Science*, *35*, 1233–1240.

Corless, R. M., G. H. Gonnet, D. E. G. Hare, D. J. Jeffrey, and D. E. Knuth (1996), On the Lambert W Function, *Adv. Comput. Math.*, *5*, 329–359.

Dimant, Y. S., and G. M. Milikh (2003), Model of anomalous electron heating in the E region: 1. Basic theory, *J. Geophys. Res.*, *108*, CiteID 1350, doi: 10.1029/2002JA009524.

Dimant, Y. S., and M. M. Oppenheim (2004), Ion thermal effects on E-region instabilities: linear theory, *J. Atmos. Terr. Phys.*, *66*, 1639–1654.

Dyrud, L. P., M. M. Oppenheim, and A. F. vom Endt (2001), The anomalous diffusion of meteor trails, *Geophys. Res. Lett.*, *28*, 2775–2778.

Dyrud, L. P., M. M. Oppenheim, S. Close, and S. Hunt (2002), Interpretation of non-specular radar meteor trails, *Geophys. Res. Lett.*, *29*, 2012, doi: 10.1029/2002GL015953.

Dyrud, L. P., L. Ray, M. Oppenheim, S. Close, and K. Denney (2005), Modelling high-power large-aperture radar meteor trails, *J. Atmos. Solar-Terr. Phys.*, *67*, 1171–1177, doi: 10.1016/j.jastp.2005.06.016.

Elford, W. G., and M. T. Elford (2001), The effective diffusion coefficient of meteor trails above 100 km, in *ESA SP-495: Meteoroids 2001 Conference*, pp. 357–359.

Farley, D. T. (1963), A plasma instability resulting in field-aligned irregularities in the ionosphere, *J. Geophys. Res.*, *68*, 6083–6097.

Farley, D. T. (1985), Theory of equatorial electrojet plasma waves: New developments and current status, *J. Atmos. Terr. Phys.*, *47*, 729–744.

FlexPDE (2006), *FlexPDE User Guide*, PDE Solutions Inc., URL:www.pdesolutions.com.

Galligan, D. P., G. E. Thomas, and W. J. Baggaley (2004), On the relationship between meteor height and ambipolar diffusion, *J. Atmos. Terr. Phys.*, *66*, 899–906.

Gurevich, A. V. (1978), *Nonlinear phenomena in the ionosphere*, Springer-Verlag, New York.

Gurevich, A. V., and E. E. Tsedilina (1967), Motion and spreading of inhomogeneities in a plasma, *Sov. Phys. Uspekhi*, *10*, 214–236.

Hocking, W. K. (2004), Experimental Radar Studies of Anisotropic Diffusion of High Altitude Meteor Trails, *Earth, Moon, and Planets*, *95*, 671–679.

Jones, W. (1991), Theory of diffusion of meteor trains in the geomagnetic field, *Planet. Space Sci.*, *39*, 1283–1288.

Jones, W. (1995), Theory of the initial radius of meteor trains, *Mon. Not R. Astron. Soc.*, *275*, 812–818.

Jones, W., and J. Jones (1990), Ionic diffusion in meteor trains, *J. Atmos. Terr. Phys.*, *52*, 185.

Kaiser, T. R., W. M. Pickering, and C. D. Watkins (1969), Ambipolar diffusion and motion of ion clouds in the Earth's magnetic field, *Planet. Space Sci.*, *17*, 519–552.

Kelley, M. C. (1989), *The Earth's Ionosphere*, Academic, San Diego, California.

Levitskii, S. M., N. Abdrakhmanov, and V. P. Timchenko (1982), The effect of the geomagnetic field on the diffusion of meteor trails, *Radiophysics and Quantum Electronics*, *25*, 1240–1243.

Lyatskaya, A. M., and M. P. Klimov (1988), The diffusion of the plasma column inclined at an angle to the magnetic field, *J. Atmos. Terr. Phys.*, *50*, 1007–1014.

Oppenheim, M. M., A. F. vom Endt, and L. P. Dyrud (2000), Electrodynamics of meteor trail evolution in the equatorial E-region ionosphere, *Geophys. Res. Lett.*, *27*, 3173–3176.

Oppenheim, M. M., A. F. vom Endt, and L. P. Dyrud (2000), Electrodynamics of meteor trail evolution in the equatorial E-region ionosphere, *Geophys. Res. Lett.*, *27*(19), 3173–3176.

Oppenheim, M. M., L. P. Dyrud, and L. Ray (2003a), Plasma instabilities in meteor trails: Linear theory, *J. Geophys. Res.*, *108*(2), 1063, doi: 10.1029/2002JA009548.

Oppenheim, M. M., L. P. Dyrud, and A. F. vom Endt (2003b), Plasma instabilities in meteor trails: 2-D simulation studies, *J. Geophys. Res.*, *108*(2), 1064, doi: 10.1029/2002JA009549.

Pickering, W. M., and D. W. Windle (1970), The diffusion of meteor trains, *Planet. Space Sci.*, *18*, 1153–1161.

Robson, R. E. (2001), Dispersion of meteor trails in the geomagnetic field, *Phys. Rev. E*, *63*(2), 026404, doi: 10.1103/PhysRevE.63.026404.

Rozhanskii, V. A., and L. D. Tsendin (1975), Spreading of a small inhomogeneity in an unbounded, weakly ionized plasma in a magnetic field, *Soviet Journal of Plasma Physics*, *1*, 944–954.

Rozhansky, V. A., and L. D. Tsendin (2001), *Transport Phenomena in Partially Ionized Plasma*, Taylor & Francis, London-New York.

Schilling, D. L. (1993), *Meteor Burst Communications*, Wiley, New York.

Simon, A. (1955a), Ambipolar Diffusion in a Magnetic Field, *Physical Review*, *98*, 317–318, doi: 10.1103/PhysRev.98.317.

Simon, A. (1955b), Diffusion of Like Particles Across a Magnetic Field, *Physical Review*, *100*, 1557–1559, doi: 10.1103/PhysRev.100.1557.

Zhou, Q. H., J. D. Mathews, and T. Nakamura (2001), Implications of meteor observations by the MU radar, *Geophys. Res. Lett.*, *28*, 1399–1402.

Y. S. Dimant, Center for Space Physics, Boston University, 725 Commonwealth Ave, Boston, MA 02215, USA (dimant@bu.edu)

This preprint was prepared with AGU's LaTeX macros v5.01, with the extension package 'AGU^{++}' by P. W. Daly, version 1.6b from 1999/08/19.